

Reducing high carrier concentration in rocksalt- $\text{Al}_x\text{Sc}_{1-x}\text{N}$ with Mg acceptor doping

EP

Cite as: Appl. Phys. Lett. **118**, 202107 (2021); <https://doi.org/10.1063/5.0052877>

Submitted: 02 April 2021 . Accepted: 04 May 2021 . Published Online: 20 May 2021

 Krithika Upadhyaya,  Dheemahi Rao,  Bidesh Biswas,  Rajendra Kumar,  Vijay Bhatia,  Ashalatha Indiradevi Kamalasanan Pillai,  Magnus Garbrecht, and  Bivas Saha

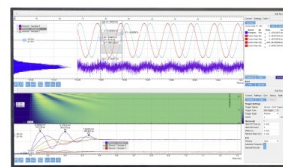
COLLECTIONS

 This paper was selected as an Editor's Pick

[View Online](#)[Export Citation](#)[CrossMark](#)

Challenge us.

What are your needs for periodic signal detection?



Zurich
Instruments

Reducing high carrier concentration in rocksalt- $\text{Al}_x\text{Sc}_{1-x}\text{N}$ with Mg acceptor doping

Cite as: Appl. Phys. Lett. **118**, 202107 (2021); doi: [10.1063/5.0052877](https://doi.org/10.1063/5.0052877)

Submitted: 2 April 2021 · Accepted: 4 May 2021 ·

Published Online: 20 May 2021



View Online



Export Citation



CrossMark

Krithika Upadhyay,^{1,2}  Dheemahi Rao,^{1,2,3}  Bidesh Biswas,^{1,2,3}  Rajendra Kumar,^{1,2}  Vijay Bhatia,⁴ 
Ashalatha Indiradevi Kamalasanan Pillai,⁴  Magnus Garbrecht,⁴  and Bivas Saha^{1,2,3,a)} 

AFFILIATIONS

¹Chemistry and Physics of Materials Unit, Jawaharlal Nehru Centre for Advanced Scientific Research, Bangalore 560064, India

²International Centre for Materials Science, Jawaharlal Nehru Centre for Advanced Scientific Research, Bangalore 560064, India

³School of Advanced Materials (SAMat), Jawaharlal Nehru Centre for Advanced Scientific Research, Bangalore 560064, India

⁴Australian Centre for Microscopy and Microanalysis, The University of Sydney, Camperdown NSW 2006, Australia

^{a)} Author to whom correspondence should be addressed: bsaha@jncasr.ac.in and bivas.mat@gmail.com

ABSTRACT

Aluminum scandium nitride ($\text{Al}_x\text{Sc}_{1-x}\text{N}$) is an emerging III-nitride semiconductor that has attracted significant interest in recent years in surface and bulk acoustic resonators for its high piezoelectric coefficient and applications in high-power electronic devices. $\text{Al}_x\text{Sc}_{1-x}\text{N}$ stabilizes in the rock salt phase for $x < 0.52$ when deposited directly on (001) MgO substrates and has been utilized as a semiconductor in single-crystalline $\text{TiN}/\text{Al}_x\text{Sc}_{1-x}\text{N}$ metal/semiconductor superlattices for thermionic energy conversion, optical hyperbolic metamaterials, and the fundamental studies on heat and current transport in materials. However, due to the presence of oxygen impurities and native defects, such as nitrogen vacancies, sputter-deposited rock salt- $\text{Al}_x\text{Sc}_{1-x}\text{N}$ exhibits a high carrier concentration in the $(2-4) \times 10^{20} \text{ cm}^{-3}$ range that leads to its Ohmic tunneling contact with metals and prevents observation of thermionic emission. In this Letter, we demonstrate that magnesium (Mg) acts as an efficient hole-dopant in $r\text{-Al}_x\text{Sc}_{1-x}\text{N}$, increases its resistivity, and reduces its carrier concentration as a function of Mg concentration to as low as $1.4 \times 10^{18} \text{ cm}^{-3}$. A combination of spectroscopy, microscopy, and first-principles modeling demonstrate (a) epitaxial 001 oriented $\text{Al}_x\text{Sc}_{1-x}\text{N}:\text{Mg}$ growth for the first 35–75 nm and subsequent pyramidal growth with multiple in-plane orientations, (b) Mg_xN_y to form a uniform and homogeneous solid solution with $r\text{-Al}_x\text{Sc}_{1-x}\text{N}$ without any precipitation, phase separation, or secondary phase formation, and (c) Mg-defect states are located deep inside the valence and conduction bands that leave behind a pristine $r\text{-Al}_x\text{Sc}_{1-x}\text{N}$ bandgap and band edges. The demonstration of Mg-hole doping in $r\text{-Al}_x\text{Sc}_{1-x}\text{N}$ marks significant progress in $r\text{-Al}_x\text{Sc}_{1-x}\text{N}$ thin film and superlattice-based devices.

Published under an exclusive license by AIP Publishing. <https://doi.org/10.1063/5.0052877>

Aluminum scandium nitride ($\text{Al}_x\text{Sc}_{1-x}\text{N}$) is an artificially structured III-V semiconducting solid-state alloy and is promising for a wide range of energy harvesting applications^{1–3} such as piezoelectrics, thermoelectrics, and as a spacer between metallic layers in plasmonic devices.⁴ Recently, $\text{Al}_x\text{Sc}_{1-x}\text{N}$ has also demonstrated ferroelectric properties that could be utilized for memory applications as well as ferroelectric gates in CMOS transistors to reduce the operating voltage.⁵ Much of the studies in recent years on $\text{Al}_x\text{Sc}_{1-x}\text{N}$ have focused on exploring the piezoelectric response of wurtzite- $\text{Al}_x\text{Sc}_{1-x}\text{N}$ solid solution alloys, which exhibits about a 400% increase in longitudinal piezoelectric coefficient compared to the well-established piezoelectric $w\text{-AlN}$.^{6,7} $w\text{-Al}_x\text{Sc}_{1-x}\text{N}$ is also actively researched for bulk acoustic wave (BAW) and surface acoustic wave (SAW) devices^{8–10} for their efficient transmission properties as well as larger electromechanical

coupling coefficient (K^2).^{11,12} $w\text{-Al}_x\text{Sc}_{1-x}\text{N}$ alloys are found to exhibit a high pyroelectric coefficient compared to AlN, which makes them potential candidates for uncooled pyroelectric infrared sensors^{13,14} as well. Recently, $\text{Al}_x\text{Sc}_{1-x}\text{N}/\text{GaN}$ heterostructures have been also explored for the development of high power and high-frequency electronic devices.¹⁵ With an objective to study, the key parameters related to the mechanical properties of microelectromechanical systems (MEMS), the coefficient of thermal expansion and elastic moduli of $w\text{-Al}_x\text{Sc}_{1-x}\text{N}$ have been determined, which show $w\text{-Al}_x\text{Sc}_{1-x}\text{N}$'s potential for radio frequency MEMS^{16,17} applications. Besides, flexible $w\text{-Al}_x\text{Sc}_{1-x}\text{N}$ films have been developed that are of significant interest due to their biocompatibility and can serve as an attractive biosensing component suitable for fabricating implantable devices for next-generation MEMS¹⁸ technologies.

A considerable amount of research has been performed in varying the Sc concentration inside the AlN matrix to understand the phase stability and phase transformation phenomenon^{19–21} in $\text{Al}_x\text{Sc}_{1-x}\text{N}$. At lower Al ($x < 0.52$) concentration, $\text{Al}_x\text{Sc}_{1-x}\text{N}$ alloys stabilize in the rock salt phase when deposited directly on MgO (001) substrates. However, the stability of the $r\text{-Al}_x\text{Sc}_{1-x}\text{N}$ phase was extended from $x \sim 0.51$ to $x \sim 0.81$ by inserting a 20 nm TiN buffer layer between the $\text{Al}_x\text{Sc}_{1-x}\text{N}$ and MgO substrate,²² with the TiN layer serving as a lattice and polarity-matching substrate. For high Al concentration, $\text{Al}_x\text{Sc}_{1-x}\text{N}$ films almost always exhibit wurtzite crystal structure.^{23–25} However, compared to the $w\text{-Al}_x\text{Sc}_{1-x}\text{N}$, $r\text{-Al}_x\text{Sc}_{1-x}\text{N}$ alloy has not received much attention. $r\text{-Al}_x\text{Sc}_{1-x}\text{N}$ has been used in recent years as a semiconducting component for the development of epitaxial lattice-matched TiN/ $\text{Al}_x\text{Sc}_{1-x}\text{N}$ metal/semiconductor superlattices for thermoelectric energy conversion devices.^{26–30} Due to its tunable lattice parameters, $r\text{-Al}_x\text{Sc}_{1-x}\text{N}$ can also be lattice-matched with several other transition metal nitrides, such as CrN, HfN, NbN, for the development of single-crystalline metal/semiconductor superlattice heterostructure. In addition to being utilized as a semiconducting component, $r\text{-Al}_x\text{Sc}_{1-x}\text{N}$ also plays a crucial role as a low-loss dielectric medium in epitaxial TiN/ $\text{Al}_x\text{Sc}_{1-x}\text{N}$ superlattices for optical hyperbolic metamaterials^{4,30} and subsequent demonstration of the photonic density of states engineering.⁴ On the whole, ample scope offered by $r\text{-Al}_x\text{Sc}_{1-x}\text{N}$ such as tunable electronic properties, lattice constant, bandgap, and dielectric permittivity makes it an interesting material to investigate and develop the practical application in devices.

For the epitaxial growth of $\text{Al}_x\text{Sc}_{1-x}\text{N}$, DC/RF magnetron sputtering^{22,31} technique is widely used. In some of the previous studies, molecular beam epitaxy (MBE),³² and metal-organic chemical vapor deposition (MOCVD)³³ have also been utilized to deposit $\text{Al}_x\text{Sc}_{1-x}\text{N}$ films on Si, Al_2O_3 , MgO substrates. Sputter-deposited $r\text{-Al}_x\text{Sc}_{1-x}\text{N}$ films ($0 < x < 0.52$) act as a degenerate n -type semiconductor with high carrier concentration in the $(2\text{--}4) \times 10^{20} \text{ cm}^{-3}$ range²² due to the incorporation of oxygen during growth as impurities^{22,34} as well as the native defects, such as nitrogen vacancies. Although such high carrier concentration could lead to an enhanced thermoelectric power factor, it prevents at the same time the use of $r\text{-Al}_x\text{Sc}_{1-x}\text{N}$ as a semiconducting component in metal/semiconductor superlattices intended for thermionic emission devices. Large carrier concentration in semiconductors leads to small depletion widths at metal/semiconductor interfaces which results in Ohmic tunneling contacts. As superlattice-based highly efficient thermoelectric material is required to exhibit a high Seebeck coefficient and electrical conductivity with moderate carrier concentration,³⁵ the achievement of thermionic emission is essential for device functionalities. Therefore, it is necessary to reduce the carrier concentration of $r\text{-Al}_x\text{Sc}_{1-x}\text{N}$ alloys. Mg_xN_y is known to act as an efficient hole dopant in reducing carrier concentration in several nitrides and alloys, including ScN,^{35,36} InN.³⁷ The previous work on Mg-doped ScN thin films has demonstrated a reduction of its carrier concentration and eventually p -type ScN.³⁶ Electronic structure calculations also showed that Mg acceptor states are located within the band and do not localize at the bandgap which allows for continuous tuning of ScN's carrier density with Mg concentration.³⁸

In this work, Mg-hole doping is introduced in sputter-deposited $r\text{-Al}_x\text{Sc}_{1-x}\text{N}$ solid solution films. Mg doping is found to reduce the carrier concentration in $r\text{-Al}_x\text{Sc}_{1-x}\text{N}$ without any phase separation, precipitation, or secondary phase formation. All $r\text{-Al}_x\text{Sc}_{1-x}\text{N}$ and

$r\text{-Al}_x\text{Sc}_{1-x}\text{N}:\text{Mg}$ (with Mg concentration 0.72%, 1.1%, 1.2%, and 1.4%) films with a thickness of ~ 200 nm are deposited using reactive DC-magnetron sputtering in a load-locked turbo-molecular pumped high vacuum deposition system with a base pressure of 2×10^{-9} Torr and substrate temperature of 750°C . A combination of Transmission Kikuchi Diffraction (TKD) and High Resolution (Scanning)/Transmission Electron Microscopy (HR(S)/TEM) and STEM Energy-dispersive x-ray spectroscopy (STEM-EDS) was adopted for the microstructural analysis. Electronic and thermoelectric properties of the films were characterized using 4-probe Hall measurement and thermoelectric characterization techniques. Finally, a detailed first-principles modeling analysis is performed to understand the impact of Mg doping on the electronic structure of $r\text{-Al}_x\text{Sc}_{1-x}\text{N}$. Details about the growth, characterization, and modeling analysis are presented in the [supplementary material](#) section.

Symmetric $2\theta\text{-}\omega$ high-resolution x-ray diffractogram (HRXRD) (see Fig. S1 in [supplementary material](#)) reveals that $r\text{-Al}_{0.55}\text{Sc}_{0.45}\text{N}$ and $r\text{-Al}_{0.55}\text{Sc}_{0.45}\text{N}:\text{Mg}$ films grow with 002 orientations on (001) MgO substrates. The main 002 peaks of $r\text{-Al}_{0.55}\text{Sc}_{0.45}\text{N}$ and $r\text{-Al}_{0.55}\text{Sc}_{0.45}\text{N}:\text{Mg}$ (representative of all other films) appear at 41.1° and 41.2° , yielding an out-of-plane lattice constant (c) of 4.39 \AA and 4.38 \AA , respectively. The closely matched lattice parameters indicate that Mg-dopant incorporation inside the $r\text{-Al}_{0.55}\text{Sc}_{0.45}\text{N}$ matrix does not influence its structural properties significantly. However, the crystalline quality of the films characterized by the full-width-at-half-maxima (FWHM) of the ω -scan (rocking curve) shows slight improvement indicated by values of 1.74° for $r\text{-Al}_{0.55}\text{Sc}_{0.45}\text{N}$ and 1.11° for the $r\text{-Al}_{0.55}\text{Sc}_{0.45}\text{N}:\text{Mg}$ film. It is important to note that the lattice constant and orientation closely matches with the previous report of $r\text{-Al}_{0.51}\text{Sc}_{0.49}\text{N}$.²²

While the symmetric $2\theta\text{-}\omega$ HRXRD measurements revealed out-of-plane lattice constant (c) and orientation, to achieve a full 3D crystallographic orientation of grain information, TKD analysis is performed on $r\text{-Al}_{0.55}\text{Sc}_{0.45}\text{N}:\text{Mg}$ film with Mg concentration of 1.4 atomic %. The (001) pole figure [see Fig. 1(a)] shows the brightest spots aligning closely with the X, Y, and Z directions, with less intense spots appearing off axes. The analysis of the brightest spots in the pole figure relates to the (001) planes in the epitaxial growth region of the film along the [001] direction of the MgO substrate. However, a set of six relatively less intense spots in the pole figure that span a range of orientations away from (001), relative to the growth direction, are found to be located between (101) and (111) are highlighted in Fig. 1(b). These spots are grouped and assigned to their respective inverse pole figure (IPF) maps marked I–VI, which represents their real-space distribution. IPF maps of the whole film shown in Fig. 1(c) emphasize the epitaxial region of growth in red and the region containing misoriented or broken grains represented in different shades of blue. Out of which, I, II, III, and, IV [see Fig. 1(I–IV)] corresponds to broken grains, whereas V and VI to the outlier grains [see Fig. 1(V–VI)], all of which are tilted and rotated with respect to the substrate. The broken grains I to IV shown in IPF maps have angular distribution between $56^\circ\text{--}60^\circ$ which is very similar to the distribution range obtained in one of the recent works on the growth of ScN epitaxial films.³⁹ However, the outlier grains V and VI are situated at $53^\circ\text{--}54^\circ$ and 44° , respectively, with respect to the substrate. Such orientation distribution obtained for a different set of grains represents their preferential growth orientation and their departure from the epitaxial growth.

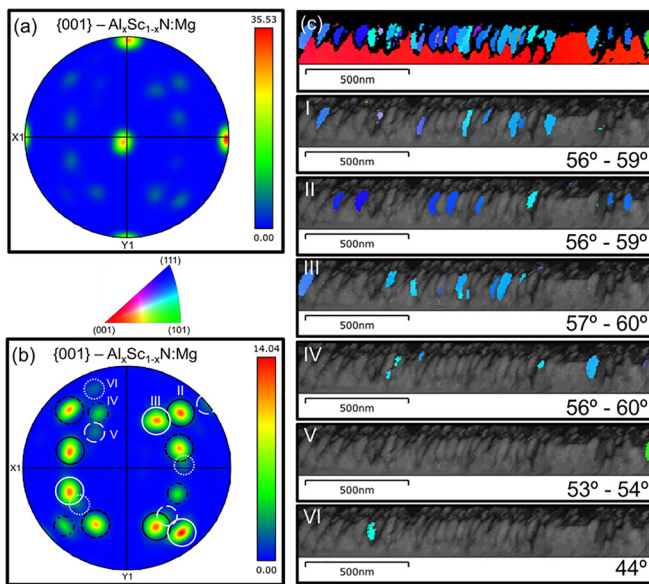


FIG. 1. (a) Transmission Kikuchi Diffraction (TKD) pole figures of Mg-doped (1.4%) $r\text{-Al}_{0.55}\text{Sc}_{0.45}\text{N}$ film where the highlighted bright main hotspots correspond to the (001) growth orientation on (001) MgO substrate. (b) A set of 6 hotspots shown more clearly in the TKD pole figure map highlighting the misorientation of grains in the broken epitaxy region. (c) Inverse pole figure (IPF) map that shows both the epitaxial region (red) as well as broken epitaxial grains of the film (I to VI). Each of the six sets of spots shown from I to VI corresponds to the group of various angular distribution from 44° – 60° of grains that are oriented between $\{101\}$ and $\{111\}$.

Therefore, from the TKD analysis, it is clear that the $r\text{-Al}_{0.55}\text{Sc}_{0.45}\text{N}$ film grows with cubic epitaxy for the first 35–75 nm from the MgO (001) substrate, subsequent to which the epitaxy breaks with multiple in-plane rotated orientations.

Microstructural analysis of the $r\text{-Al}_{0.55}\text{Sc}_{0.45}\text{N}$:Mg (1.4%) film was carried out using HR(S)/TEM. From the cross-sectional overview STEM image [see Fig. 2(a)], the growth of the film can be described by differentiating it into two regions. In region-I, the film maintains the (001)[001] $r\text{-Al}_{0.55}\text{Sc}_{0.45}\text{N}$:Mg || (001)[001] MgO epitaxial relationship with the substrate, which can also be observed from the electron diffraction pattern showing cubic diffraction pattern in the inset of Fig. 2(a). The region-I starts at the film/substrate interface and extends to the surface of the film in some areas [left of Fig. 2(a)], whereas, in other areas, pyramidal growth appears with broken epitaxy beyond the side facets (region-II). In some cases, the pyramidal growth starts already at the substrate film interface [see Fig. 2(b)], with angles corresponding to mostly low-index sets of planes forming the pyramids side facets. For instance, the side facets of the pyramids form an angle -72° , $+63^\circ$ [see Fig. 2(a)], and $+54^\circ$ [see Fig. 2(b)] with the substrate corresponding to (103), (102), and (111) planes, respectively. The high-resolution STEM micrograph in Fig. 2(c) demonstrates the sharp $\text{Al}_x\text{Sc}_{1-x}\text{N}$:Mg/MgO interface with the presence of misfit dislocation attributed to the lattice-mismatch ($\sim 4\%$) between substrate and film.

In region-II, the epitaxy is broken with multiple in-plane orientations due to lower adatom mobility to overcome the Ehrlich-Schwoebel (E-S) barrier³⁹ from insufficient substrate temperature. As a result, the epitaxial relationship between the $r\text{-Al}_{0.55}\text{Sc}_{0.45}\text{N}$:Mg

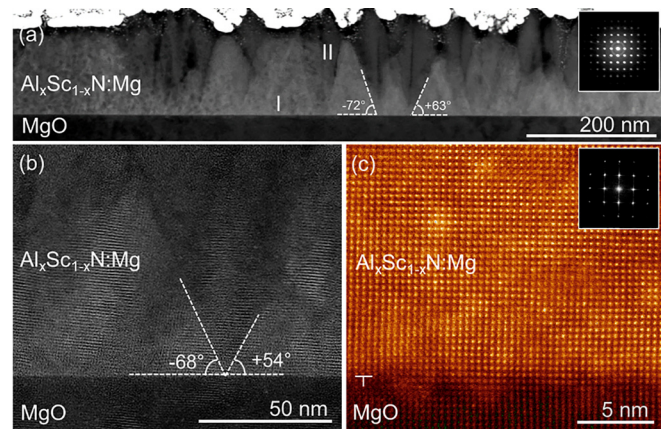


FIG. 2. (a) Overview STEM micrograph of the $\text{Al}_{0.55}\text{Sc}_{0.45}\text{N}$:Mg (1.4%) film deposited on (001) MgO substrate and electron diffraction pattern of the substrate and the film as inset. (b) STEM image highlighting the pyramidal growth originating from the film-substrate interface. (c) High-resolution STEM micrograph and FFT highlights the epitaxial growth of the film through its FFT (see inset).

(1.4%) film and the MgO substrate breaks completely in region-II which displays a high concentration of defects [Fig. 2(a)]. The pyramidal structures on the surface of the film are shown as well in plan-view scanning electron microscopy (SEM) in supplementary material Fig. S2. The origin of this type of microstructure in similar pure ScN films is discussed in detail elsewhere.³⁹

STEM-EDS mapping was further employed, as some regions close to the top surface of the film containing pronounced defects appeared dark in HAADF-STEM contrast [Fig. 3(a)]. The elemental mapping of Al, Sc, and N [see Figs. 3(b), 3(c), and 3(e)] shows their uniform elemental distribution throughout the film except in the regions containing the voids which are depleted of atoms. However, excess of O can be found to accumulate in these voids [Fig. 3(f)].⁴⁰ Also, a 1.4 atomic % Mg concentration is determined from quantitative analysis of the integrated EDS maps⁴¹ which appears homogeneously spread across the film [see Fig. 3(d)], indicating that Mg_xN_y makes a uniform solid solution without any precipitation, phase separation, or secondary phase formation. As the films are deposited on MgO substrates, traditional quantitative metrology techniques such as Rutherford Back Scattering spectroscopy are not suitable for the determination of Mg concentration in the films. Therefore, the STEM-EDS analysis is used to benchmark the composition of other films.

Electronic properties of both undoped and Mg-doped $r\text{-Al}_{0.55}\text{Sc}_{0.45}\text{N}$ thin-film alloys across the compositional range were measured at room temperature using a 4-probe Hall measurement system [presented in Fig. 4(a)]. The resistivity of the undoped $r\text{-Al}_{0.55}\text{Sc}_{0.45}\text{N}$ alloy was found to be $58.8\text{ m}\Omega\text{-cm}$ and increased with an increase in the Mg doping concentration. It is important to note that the $r\text{-Al}_{0.55}\text{Sc}_{0.45}\text{N}$ thin films are about $100\times$ more resistive compared to undoped ScN films primarily due to the decrease in mobility due to alloy scattering. $r\text{-Al}_{0.55}\text{Sc}_{0.45}\text{N}$ doped with the highest Mg concentration (1.4%) exhibits the highest resistivity of $1.211\text{ }\Omega\text{-cm}$, which is about $20\times$ higher than that of the undoped film. Undoped $r\text{-Al}_{0.55}\text{Sc}_{0.45}\text{N}$ film exhibits a high n -type carrier concentration of $\sim 1.1 \times 10^{20}\text{ cm}^{-3}$ due to the unintentional n -type doping by unwanted oxygen impurities and

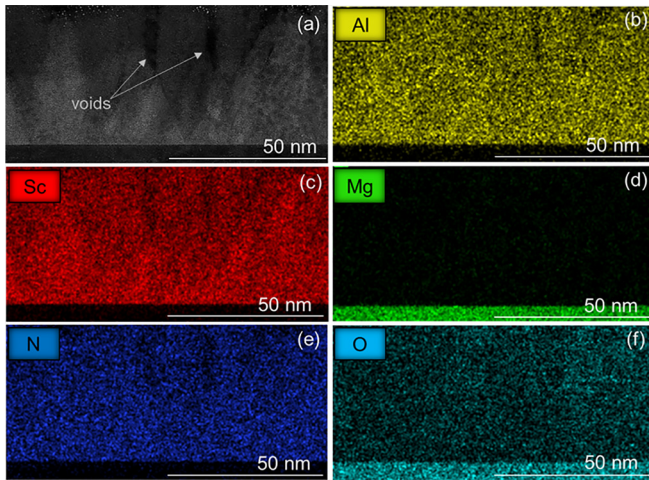


FIG. 3. (a) HAADF-STEM image of $\text{Al}_{0.55}\text{Sc}_{0.45}\text{N}:\text{Mg}$ (1.4%) film and its corresponding STEM-EDS elemental maps (b) Al, (c) Sc, (d) Mg, (e) N, and (f) O are shown. Voids in the defect regions (marked) are found to be depleted of Al, Sc, and N atoms, but rich in oxygen atoms. Mg is distributed homogeneously throughout the film without any phase separation, precipitation or secondary phase formation.

native defects such as nitrogen vacancies. The carrier concentration observed here is in a very similar range as that in a previous report on $\text{Al}_x\text{Sc}_{1-x}\text{N}$ solid solution,²² as well as that of undoped ScN thin films.^{42–44} However, the carrier concentration shows a significant reduction from $\sim 1.1 \times 10^{20} \text{ cm}^{-3}$ to $\sim 1.4 \times 10^{18} \text{ cm}^{-3}$ with the incorporation of Mg inside the $\text{Al}_{0.55}\text{Sc}_{0.45}\text{N}$ matrix. This result emphasizes the role played by Mg in acting as an efficient hole-dopant in effectively reducing the carrier concentration. The mobility of the films is rather low due to the large alloy scattering effects. Previous calculations⁴¹ have revealed a depletion width of more than 10–15 nm at a metal/semiconductor contact when the carrier density is reduced to less than $1 \times 10^{18} \text{ cm}^{-3}$.²⁸ Therefore, $r\text{-Al}_{0.55}\text{Sc}_{0.45}\text{N}$ doped with an Mg

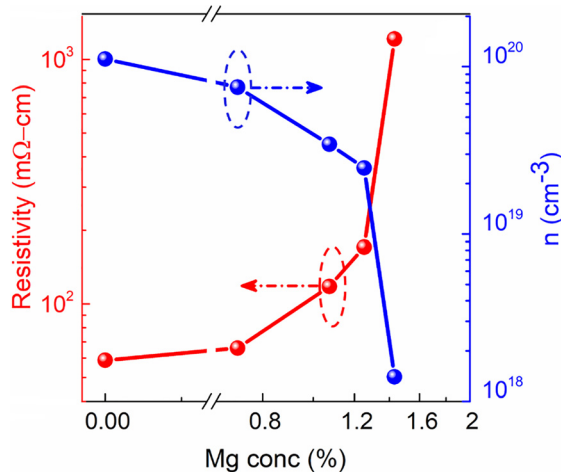


FIG. 4. Room temperature resistivity and carrier concentration (n) as the function of Mg concentration in $r\text{-Al}_{0.55}\text{Sc}_{0.45}\text{N}$ matrix. With an increase in Mg concentration, the resistivity was found to increase, while the carrier concentration decreased due to the acceptor nature of Mg inside $r\text{-Al}_{0.55}\text{Sc}_{0.45}\text{N}$.

concentration (1.4%) should be ideal for developing metal/ $r\text{-Al}_{0.55}\text{Sc}_{0.45}\text{N}:\text{Mg}$ superlattices with thermionic emission properties.

To understand the nature of the compensation effect, the electronic structure of undoped and Mg-doped $r\text{-Al}_{0.55}\text{Sc}_{0.45}\text{N}$ with an Mg concentration of $\sim 1.56\%$ are calculated within the density functional theory (DFT) modelling^{45,46} (see [supplementary material](#) for details). To reduce the number of atoms in the supercell and associated computational cost, all calculations are performed with $x=0.5$ in $\text{Al}_x\text{Sc}_{1-x}\text{N}$, even though experimentally x was measured to be 0.55. Undoped $r\text{-Al}_{0.5}\text{Sc}_{0.5}\text{N}$ exhibits a bandgap of 0.68 eV without any bandgap correction [see [Fig. 5\(a\)](#)]. As conventional DFT underestimates the bandgap of semiconductors, it is not surprising. A Hubbard U correction with $U=3.5 \text{ eV}$ on Sc-3d orbitals was employed to correct the bandgap issue that resulted in a gap of 1.44 eV [see [Figs. 5\(a\)](#) and [5\(c\)](#)] which is still underestimated by $\sim 43\%$ with respect to experimental results. Such underestimation of bandgap even with the Hubbard U correction can be attributed to the presence of Al-3s and Al-3p states, which cannot be corrected with the Hubbard U correction. Partial densities of electronic states ($p\text{DOS}$) show [see [Figs. 5\(b\)](#) and [5\(d\)](#)] that Mg incorporation does not give rise to any defect states inside the bandgap of $\text{Al}_{0.5}\text{Sc}_{0.5}\text{N}$. The Mg-2p states are almost negligible near the valence band edge (the $p\text{DOS}$ plot of Mg-2p is multiplied by 3000), whereas Mg-3s states mainly appear deep in the valence band $\sim 4 \text{ eV}$ below the valence band edge, which suggests that the pristine bandgap of $r\text{-Al}_{0.5}\text{Sc}_{0.5}\text{N}$, as well as the band edges (which are important for electronic transport), remains intact upon Mg incorporation. The Fermi level shifts inside the valence band indicating the acceptor nature of Mg dopants in $r\text{-Al}_{0.5}\text{Sc}_{0.5}\text{N}$, which results in the compensation of donors formed due to oxygen impurities and/or nitrogen vacancies. Therefore, the monotonic increase in resistivity and decrease in the carrier concentration of $r\text{-Al}_{0.55}\text{Sc}_{0.45}\text{N}$ with an increase in Mg concentration can be attributed to the acceptor nature of Mg that leaves the rigid band electronic structure of $r\text{-Al}_x\text{Sc}_{1-x}\text{N}$

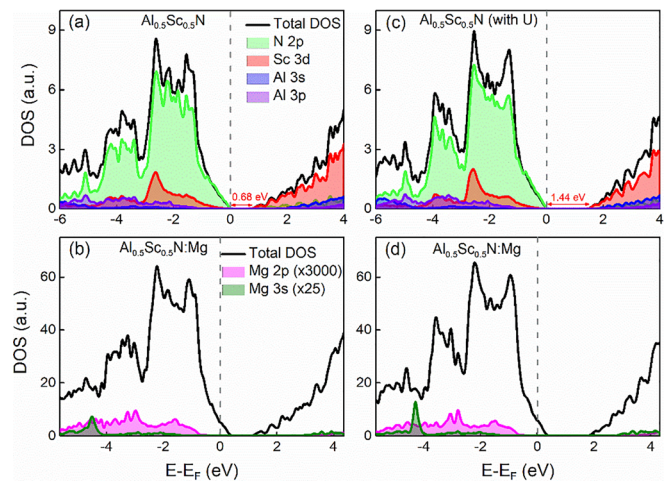


FIG. 5. Total and partial electronic density of states of (a) $\text{Al}_{0.5}\text{Sc}_{0.5}\text{N}$ and (b) $\text{Al}_{0.5}\text{Sc}_{0.5}\text{N}:\text{Mg}$ without Hubbard U correction which shows that Mg-defect states lie deep inside the valence and conduction bands and do not change either bandgap or the band edges. Total and Mg electronic density of states of (c) $\text{Al}_{0.5}\text{Sc}_{0.5}\text{N}$ and (d) $\text{Al}_{0.5}\text{Sc}_{0.5}\text{N}:\text{Mg}$ is presented with bandgap correction in Sc-3d orbital. The bandgap is underestimated even with the Hubbard U correction.

unchanged, does not alter the valence and conduction band edges, and allows for a free movement of Fermi level. While the reduced carrier concentration of $1.4 \times 10^{18} \text{ cm}^{-3}$ in $r\text{-Al}_x\text{Sc}_{1-x}\text{N}:\text{Mg}$ films seems ideal for the development of metal/semiconductor superlattices for thermionic energy conversion, temperature-dependent electrical conductivity, Seebeck coefficient, and power factor of the $r\text{-Al}_x\text{Sc}_{1-x}\text{N}:\text{Mg}$ films are measured further (see [supplementary material](#)).

In conclusion, Mg-acceptor (hole) doping is used to reduce the carrier concentration of $r\text{-Al}_{0.55}\text{Sc}_{0.45}\text{N}$ alloys for its potential thermionic energy conversion application in metal/semiconductor superlattice devices. Mg_xN_y is found to be an efficient hole-dopant in $r\text{-Al}_{0.55}\text{Sc}_{0.45}\text{N}$ alloys and does not exhibit any phase separation, precipitation or secondary phase formation. Theoretical calculations revealed that Mg-defect states are located within the bands that leave a pristine $r\text{-Al}_{0.55}\text{Sc}_{0.45}\text{N}$ bandgap and band edges unchanged. Due to the compensation effect, the carrier concentration of $r\text{-Al}_{0.55}\text{Sc}_{0.45}\text{N}$ was reduced from $1.1 \times 10^{20} \text{ cm}^{-3}$ to as low as $1.4 \times 10^{18} \text{ cm}^{-3}$. The development of hole-doped $r\text{-Al}_x\text{Sc}_{1-x}\text{N}$ with reduced carrier concentration marks significant progress in the research of cubic nitride semiconductors and will help develop thermionic emission devices with improved efficiencies.

See the [supplementary material](#) for information related to the growth process, HRXRD, SEM, TKD, and HRTEM characterization, thermoelectric measurement, and details related to the first-principles modeling.

K.U. and B.S. acknowledge support from the International Centre for Materials Science (ICMS) and Sheikh Saqr Laboratory (SSL) of the Jawaharlal Nehru Centre for Advanced Scientific Research (JNCASR). BS acknowledges Young Scientist Research Award (YSRA) from the Board of Research in Nuclear Sciences (BRNS), Department of Atomic Energy (DAE), India with Grant No. 59/20/10/2020-BRNS/59020 for financial support. The authors acknowledge the facilities of Sydney Microscopy and Microanalysis at The University of Sydney.

DATA AVAILABILITY

The data that support the findings of this study are available from the corresponding author upon reasonable request.

REFERENCES

- R. Matloub, M. Hadad, A. Mazzalai, N. Chidambaram, G. Moulard, C. S. Sandu, T. Metzger, and P. Murali, *Appl. Phys. Lett.* **102**, 152903 (2013).
- S. Barth, H. Bartzsch, D. Glöf, P. Frach, T. Modes, O. Zywitzki, G. Suchanek, and G. Gerlach, *Microsyst. Technol.* **22**, 1613 (2016).
- P. Frach, S. Barth, H. Bartzsch, and D. Gloess, *Proc. SPIE* **10194**, 101942Z (2017).
- G. V. Naik, B. Saha, J. Liu, S. M. Saber, E. A. Stach, J. M. K. Irudayaraj, T. D. Sands, V. M. Shalae, and A. Boltasseva, *Proc. Natl. Acad. Sci. U. S. A.* **111**, 7546 (2014).
- S. Fichtner, N. Wolff, F. Lofink, L. Kienle, and B. Wagner, *J. Appl. Phys.* **125**, 114103 (2019).
- M. Akiyama, T. Kamohara, K. Kano, A. Teshigahara, Y. Takeuchi, and N. Kawahara, *Adv. Mater.* **21**, 593 (2009).
- F. Tasnádi, B. Alling, C. Höglund, G. Wingqvist, J. Birch, L. Hultman, and I. A. Abrikosov, *Phys. Rev. Lett.* **104**, 137601 (2010).
- V. Pashchenko, R. Matloub, F. Parsapourkoulour, P. Murali, S. Ballandras, and K. Haffner, in *IEEE International Ultrasonics Symposium* (IEEE, 2016), pp. 1–4.
- M. Moreira, J. Bjurström, I. Katardjev, and V. Yantchev, *Vacuum* **86**, 23 (2011).
- A. Teshigahara, K. Hashimoto, and M. Akiyama, in *IEEE International Ultrasonics Symposium* (IEEE, 2012), pp. 1–5.
- K. Umeda, H. Kawai, A. Honda, M. Akiyama, T. Kato, and T. Fukura, in *IEEE 26th International Conference MicroElectroMechanical Systems* (IEEE, 2013), pp. 733–736.
- G. Wingqvist, F. Tasnádi, A. Zukauskaitė, J. Birch, H. Arwin, and L. Hultman, *Appl. Phys. Lett.* **97**, 112902 (2010).
- V. Vasilyev, J. Cetnar, B. Clafin, G. Grzybowski, K. Leedy, N. Limberopoulos, D. Look, and S. Tetlak, *MRS Adv.* **1**, 2711 (2016).
- D. K. T. Ng, T. Zhang, L. Y. Siow, L. Xu, C. P. Ho, H. Cai, L. Y. T. Lee, Q. Zhang, and N. Singh, *Appl. Phys. Lett.* **117**, 183506 (2020).
- C. Manz, S. Leone, L. Kirste, J. Ligl, K. Frei, T. Fuchs, M. Prescher, P. Waltereit, M. A. Verheijen, A. Graff, M. Simon-Najasek, F. Altmann, M. Fiederle, and O. Ambacher, *Semicond. Sci. Technol.* **36**, 034003 (2021).
- Y. Lu, M. Reusch, N. Kurz, A. Ding, T. Christoph, M. Prescher, L. Kirste, O. Ambacher, and A. Zukauskaitė, *APL Mater.* **6**, 076105 (2018).
- E. Yasar, D. Meyners, E. Quandt, S. Fichtner, P. Hayes, A. Piorra, T. Reimer, T. Lisee, P. Frank, B. Wagner, and F. Lofink, *J. Microelectromech. Syst.* **28**, 1019 (2019).
- L. Algieri, M. T. Todaro, F. Guido, L. Blasi, V. Mastronardi, D. Desmaële, A. Quattieri, C. Giannini, T. Sibillano, and M. De Vittorio, *ACS Appl. Mater. Interfaces* **12**, 18660 (2020).
- B. Saha, S. Saber, E. A. Stach, E. P. Kvam, and T. D. Sands, *Appl. Phys. Lett.* **109**, 172102 (2016).
- C. Höglund, J. Bareño, J. Birch, B. Alling, Z. Czigiány, and L. Hultman, *J. Appl. Phys.* **105**, 113517 (2009).
- R. Deng, S. R. Evans, and D. Gall, *Appl. Phys. Lett.* **102**, 112103 (2013).
- B. Saha, S. Saber, G. V. Naik, A. Boltasseva, E. A. Stach, E. P. Kvam, and T. D. Sands, *Phys. Status Solidi* **252**, 251 (2015).
- N. Wolff, S. Fichtner, B. Haas, M. R. Islam, F. Niekil, M. Kessel, O. Ambacher, C. Koch, B. Wagner, F. Lofink, and L. Kienle, *J. Appl. Phys.* **129**, 034103 (2021).
- M. Baeumler, Y. Lu, N. Kurz, L. Kirste, M. Prescher, T. Christoph, J. Wagner, A. Zukauskaitė, and O. Ambacher, *J. Appl. Phys.* **126**, 045715 (2019).
- C. Höglund, J. Birch, B. Alling, J. Bareño, Z. Czigiány, P. O. Å. Persson, G. Wingqvist, A. Zukauskaitė, and L. Hultman, *J. Appl. Phys.* **107**, 123515 (2010).
- J. L. Schroeder, B. Saha, M. Garbrecht, N. Schell, T. D. Sands, and J. Birch, *J. Mater. Sci.* **50**, 3200 (2015).
- S. Nayak, S. Acharya, M. Baral, M. Garbrecht, T. Ganguli, S. M. Shivaprasad, and B. Saha, *Appl. Phys. Lett.* **115**, 251901 (2019).
- B. Saha, A. Shakouri, and T. D. Sands, *Appl. Phys. Rev.* **5**, 021101 (2018).
- M. Garbrecht, L. Hultman, M. H. Fawey, T. D. Sands, and B. Saha, *Phys. Rev. Mater.* **1**, 033402 (2017).
- M. Garbrecht, L. Hultman, M. H. Fawey, T. D. Sands, and B. Saha, *J. Mater. Sci.* **53**, 4001 (2018).
- M. Akiyama, T. Tabaru, K. Nishikubo, A. Teshigahara, and K. Kano, *J. Ceram. Soc. Jpn.* **118**, 1166 (2010).
- M. T. Hardy, B. P. Downey, N. Nepal, D. F. Storm, D. S. Katzer, and D. J. Meyer, *Appl. Phys. Lett.* **110**, 162104 (2017).
- S. Leone, J. Ligl, C. Manz, L. Kirste, T. Fuchs, H. Menner, M. Prescher, J. Wiegert, A. Zukauskaitė, R. Quay, and O. Ambacher, *Phys. Status Solidi RRL* **14**, 1900535 (2020).
- A. le Febvrier, N. Tureson, N. Stalkerich, G. Greczynski, and P. Klund, *J. Phys. D: Appl. Phys.* **52**, 035302 (2019).
- B. Saha, J. A. Perez-Taborda, J.-H. Bahk, Y. R. Koh, A. Shakouri, M. Martin-Gonzalez, and T. D. Sands, *Phys. Rev. B* **97**, 085301 (2018).
- B. Saha, M. Garbrecht, J. A. Perez-Taborda, M. H. Fawey, Y. R. Koh, A. Shakouri, M. Martin-Gonzalez, L. Hultman, and T. D. Sands, *Appl. Phys. Lett.* **110**, 252104 (2017).
- M.-Y. Xie, N. Ben Sedrine, S. Schöche, T. Hofmann, M. Schubert, L. Hung, B. Monemar, X. Wang, A. Yoshikawa, K. Wang, T. Araki, Y. Nanishi, and V. Darakchieva, *J. Appl. Phys.* **115**, 163504 (2014).
- S. Nayak, M. Baral, M. Gupta, J. Singh, M. Garbrecht, T. Ganguli, S. M. Shivaprasad, and B. Saha, *Phys. Rev. B* **99**, 161117 (2019).

- ³⁹D. Rao, B. Biswas, S. Acharya, V. Bhatia, A. I. K. Pillai, M. Garbrecht, and B. Saha, *Appl. Phys. Lett.* **117**, 212101 (2020).
- ⁴⁰R. Kumar, S. Nayak, M. Garbrecht, V. Bhatia, A. Indiradevi Kamalasanan Pillai, M. Gupta, S. M. Shivaprasad, and B. Saha, *J. Appl. Phys.* **129**, 055305 (2021).
- ⁴¹M. Garbrecht, I. McCarroll, L. Yang, V. Bhatia, B. Biswas, D. Rao, J. M. Cairney, and B. Saha, *J. Mater. Sci.* **55**, 1592 (2020).
- ⁴²D. Gall, M. Städele, K. Järrendahl, I. Petrov, P. Desjardins, R. T. Haasch, T.-Y. Lee, and J. E. Greene, *Phys. Rev. B* **63**, 125119 (2001).
- ⁴³P. V. Burmistrova, J. Maassen, T. Favaloro, B. Saha, S. Salamat, Y. Rui Koh, M. S. Lundstrom, A. Shakouri, and T. D. Sands, *J. Appl. Phys.* **113**, 153704 (2013).
- ⁴⁴S. Kerdsonpanya, N. Van Nong, N. Pryds, A. Žukauskaitė, J. Jensen, J. Birch, J. Lu, L. Hultman, G. Wingqvist, and P. Eklund, *Appl. Phys. Lett.* **99**, 232113 (2011).
- ⁴⁵P. Giannozzi, S. Baroni, N. Bonini *et al.*, *J. Phys.: Condens. Matter* **21**, 395502 (2009).
- ⁴⁶P. Giannozzi, O. Andreussi, T. Brumme *et al.*, *J. Phys.: Condens. Matter* **29**, 465901 (2017).